FILE

INTERNAL DOCUMENT 222

I.O.S.

A numerical study of the Internal Tide at the Continental Shelf-Break

by

P D EDWARDS, A L NEW and
A D HEATHERSHAW

Internal Document No 222

NATURAL ENVIRONMENT RESEARCH COUNCIL
INSTITUTE OF OCEANOGRAPHIC SCIENCES

INSTITUTE OF OCEANOGRAPHIC SCIENCES

Wormley, Godalming,
Surrey GU8 5UB
(042-879-4141)

(Director: Dr. A. S. Laughton)

Bidston Observatory,
Birkenhead,
Merseyside L43 7RA
(051-653-8633)
(Assistant Director: Dr. D. E. Cartwright)

Crossway,
Taunton,
Somerset TA1 2DW
(0823-86211)
(Assistant Director: M. J. Tucker)

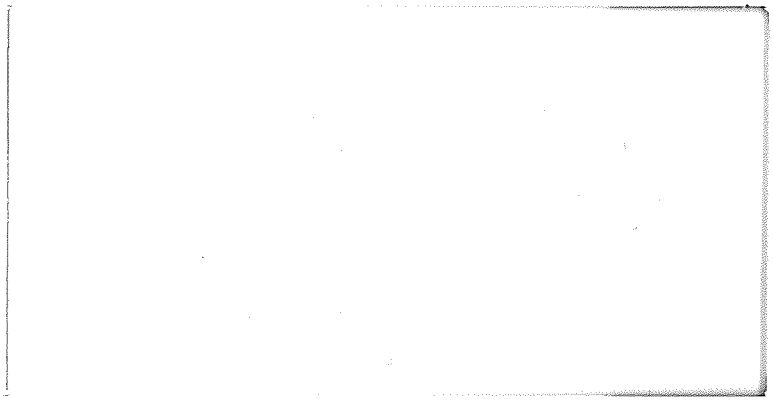

A numerical study of the Internal Tide at the Continental Shelf-Break

by

P D EDWARDS, A L NEW and
A D HEATHERSHAW

Internal Document No 222

Institute of Oceanographic Sciences
Crossway
Taunton
Somerset

October 1984

CONTENTS

1 Introduction

Pingree, Griffiths and Mardell (1983) have developed a two layer hydrostatic model to investigate observations of the internal tide which develops at the shelf break in the Celtic Sea. The work described here compares a similar model with data obtained from current meter moorings near La Chapelle Bank, and investigates some of the phenomena thought to be associated with the internal tide.

A simple approximation to the topography in the vicinity of La Chapelle Bank is adopted, and then the various parameters of the numerical calculations are adjusted, firstly to observe their effect, and then to bring the model in line with the observations. Current measurements at La Chapelle Bank (Heathershaw, 1984) have indicated the presence of a velocity surge once each tidal cycle (Fig 1). This surge is on-shelf in the upper layer, and off-shelf in the lower layer, and occurs approximately one hour after maximum flood at this position, which is about 6 km on-shelf. The present model is used to predict these surges, and to investigate how they are affected by the depth of the upper layer and the density difference between the two layers. Their effect on sediment transport at the shelf break is also investigated.

2 Methods

2.1 Assumptions used for the model

The assumption that the pressure is hydrostatic is used, and hence all vertical velocities are neglected relative to horizontal velocities and all waves are assumed to be long waves. The water column is considered to consist of two layers, the densities and velocities being considered uniform with depth in each layer. The model is fully non linear, and the barotropic M_2 tide is assumed throughout.

2.2 Equations used for modelling the system

Four hydrostatic equations, which incorporate the kinematic condition at the surface and interface, are obtained by considering the conservation of momentum and mass in each layer.

Continuity in the upper layer gives:

$$\frac{\partial}{\partial x}\left((h_1 + \zeta - \eta)u_1\right) + \frac{\partial}{\partial t}(\zeta - \eta) = 0 \qquad (1)$$

and similarly continuity in the lower layer gives:

$$\frac{\partial}{\partial x}\left((h_2 + \eta)u_2\right) + \frac{\partial \eta}{\partial t} = 0 \qquad (2)$$

Here η is the upward displacement of the interface, ζ is the upward displacement of the surface, h_i are the equilibrium depths of the layers and u_i are the fluid velocities, with subscripts $_1$ for the upper layer and $_2$ for the lower layer. Fig 2 represents these variables on a diagram of the model.

Similarly, conservation of momentum gives:

$$\frac{\partial u_1}{\partial t} + u_1 \frac{\partial u_1}{\partial x} = -g \frac{\partial \zeta}{\partial x} \qquad (3)$$

for the upper layer, and:

$$\frac{\partial u_2}{\partial t} + u_2 \frac{\partial u_2}{\partial x} = -g \frac{\rho_1}{\rho_2} \frac{\partial \zeta}{\partial x} - g \frac{\delta\rho}{\rho_2} \frac{\partial \eta}{\partial x} \qquad (4)$$

for the lower layer.

Here ρ_i are the constant densities of the two layers, and $\delta\rho$ their difference $\rho_2 - \rho_1$ ($\delta\rho$ positive for stability). The on-shelf direction is taken as positive, with x being measured from an origin on the seaward side of the shelf slope.

Now let h' be the depth of the displaced upper layer, and h'' the depth of the displaced lower layer, then we have:

$$h' = h_1 + \zeta - \eta$$

$$h'' = h_2 + \eta$$

Define $$U = \frac{h'u_1 + h''u_2}{H}$$

and $$u = u_1 - u_2$$

where $$H = h' + h''$$

Here U is the barotropic tide, and u is the shear between the layers or the baroclinic tide.

Subtracting (4) from (3) gives the "momentum" equation

$$\frac{\partial u}{\partial t} + \frac{\partial}{\partial x}(Uu) + \frac{1}{2}\frac{\partial}{\partial x}\left(u^2 \frac{(h' - h'')}{H}\right) = g\frac{\delta\rho}{\rho_2}\frac{\partial}{\partial x}(\eta - \zeta) \qquad (5)$$

However, following Pingree et al (1983), a term of the form $K_1 \frac{\partial^2 u}{\partial x^2}$ could be included in the above equation to model attenuation by viscous, or possibly turbulent, diffusion. Varying the coefficient K_1 provides a means of controlling the numerical stability of the calculations used to solve the equations. Also, a further term $-K_2 u$ could be included to represent the effects of internal friction. Finally, if we assume that the x and t derivatives of ζ are negligible compared with the corresponding derivatives of η, equation (5) becomes:

$$\frac{\partial u}{\partial t} + \frac{\partial}{\partial x}(Uu) + \frac{1}{2}\frac{\partial}{\partial x}\left(u^2 \frac{(h_2 - h_1 + 2\eta)}{H}\right) = \beta\frac{\partial \eta}{\partial x} + K_1\frac{\partial^2 u}{\partial x^2} - K_2 u \qquad (6)$$

where $\beta = \frac{g\delta\rho}{\rho_2}$, and $H = h_1 + h_2$

On subtracting the two continuity equations we obtain:

$$\frac{\partial \eta}{\partial t} = \frac{\partial}{\partial x}((h_1 - \eta)U) + \frac{\partial}{\partial x}\left(\frac{(h_1 - \eta)(h_2 + \eta)}{H} u\right), \qquad (7)$$

so that we have two equations ((6) and (7)) for the two unknowns $u(x,t)$ and $\eta(x,t)$.

(Pingree et al do not include the third term on the left hand side of equation (6), but this was found to have very little significance. See section 3.1).

2.3 Radiation conditions

It is necessary to allow waves reaching the horizontal extremities of the model to propogate out freely, and thus a radiation condition is applied at each end of the model. The radiation condition used is:

$$\frac{h_1 h_2}{H} u = \pm c\eta \qquad (8)$$

where $c^2 = \frac{g\,\delta\rho}{\rho_2}\left(\frac{h_1 h_2}{H}\right)$, ie c is the long wave phase speed, and the

sign used is minus that of the direction of propogation of the waves at the boundary. The derivation of this radiation condition requires that the sea bed be horizontal at both boundaries, and the positive direction is on-shelf.

2.4 Methods used for numerical solution

Finite difference methods are used both spatially and temporally to solve the equations (6) and (7) with boundary conditions (8) and initial conditions as specified. The initial conditions used throughout the present work are:

$$\eta(x,o) = u(x,o) = 0 \tag{9}$$

The model is forced by the semi-diurnal barotropic tide, ie $U = U_o \cos \omega t$ adjusted for each horizontal position using the continuity equation

$$\frac{\partial}{\partial x}(HU) = 0$$

which gives $U(x)\,H(x) = U_o\,H_o$

where U_o is the value U at the on-shelf end of the model and H_o is the value of H at the same point.

Equations (6) and (7) are two equations in the two unknowns $\eta(x,t)$ and $u(x,t)$. If, for the moment, the complete spatial solution is assumed to be known at some times $t = t_n$ and $t = t_n - \Delta t$ then central differences are used to advance the solution to the next timestep by a 'leapfrog' method.

The spatial derivatives on the right hand sides of equations (6) and (7) are evaluated using the central difference formulae:

$$\frac{\partial}{\partial x} f(x_o) = \frac{f(x_o + \Delta x) - f(x_o - \Delta x)}{2\Delta x} + O(\Delta x)^2 \tag{10}$$

and

$$\frac{\partial^2}{\partial x^2} f(x_o) = \frac{f(x_o + \Delta x) - 2f(x_o) + f(x_o - \Delta x)}{(\Delta x)^2} + O(\Delta x)^2 \tag{11}$$

while the left hand sides are evaluated using the central difference formulae:

$$\left.\frac{\partial \eta}{\partial t}\right|_{t_n} = \frac{\eta(t_n + \Delta t) - \eta(t_n - \Delta t)}{2\Delta t} + O(\Delta t)^2 \qquad (12)$$

and

$$\left.\frac{\partial u}{\partial t}\right|_{t_n} = \frac{u(t_n + \Delta t) - u(t_n - \Delta t)}{2\Delta t} + O(\Delta t)^2 \qquad (13)$$

The spatial grid consists of 2n + 1 points, all spaced at an equal distance Δx apart and staggered such that η and u are known at alternate positions (see Fig 3). Equations (12) and (13) are then applied to the η and u positions respectively, in order to advance to the next time level $t_n + \Delta t$. Having obtained u and η at alternate grid points at this new time level a staight-forward linear interpolation is used to evaluate each of the two variables at the intermediate points (these will be needed to step the solution forward to the next time level). Thus the grid is complete for the $n + 1^{th}$ time step.

Simons (1980) suggests that computational stability will require

$$\frac{\Delta t}{\Delta x} < \frac{1}{\sqrt{2}c_{max}}$$

and

$$\Delta t < \frac{(\Delta x)^2}{2K_1}$$

where c_{max} is the maximum long wave speed occuring in the model. Δt has been chosen in accordance with this.

2.5 Sediment transport calculations

Analysis of sediment samples from La Chapelle Bank (Heathershaw and Codd, 1984) shows that they have an overall mean grain size of approximately 500 μm. Material as coarse as this will move principally as bedload (ie grains will roll or saltate along the seabed). Bedload transport rates may be estimated using Hardisty's (1983) modified excess stress formulation of Bagnold's (1966) sediment transport equation, in which the quantity of sediment transported as bedload is given by:

$$q_{sb} = k\ (u_{100}^2 - u_{100_{CR}}^2).\ u_{100} \qquad (g\ cm^{-1}s^{-1}) \qquad (14)$$

It should be noted that for convenience and for comparisons with other work, sediment transport calculations in this section have been carried out in c.g.s. units.

In (14) k is a dimensional coefficient which depends on grain size, u_{100} is the current at 1 m above the seabed, and $u_{100_{CR}}$ is the corresponding threshold velocity. There is some uncertainty in the exact form of k but a re-evaluation of the data in Hardisty's Figure 1 and Table 1 gives

$$k = 1.773 \times 10^{-6} \, d^{-0.6916} \text{ g cm}^{-4}\text{s}^2 \qquad (15)$$

where d is the grain size in mm.

The model only provides a value of depth mean flow for the lower layer. However, a logarithmic velocity profile for the lower layer is assumed:

$$u = \frac{u_*}{\kappa} \ln \frac{z}{z_o} \qquad (16)$$

where u_* is the friction velocity, κ is the Von Karman constant equal to .4, z_o is the roughness length and z is the height above the bed. By integrating (16) over the lower layer a relationship is obtained between u_{100} and u_2, viz:

$$u_{100} = \frac{u_2}{\ln(\frac{h_2}{ez_o})} \ln (\frac{100}{z_o}) \qquad (17)$$

Equation (16) enables calculation of $u_{100_{CR}}$ from a value of the critical friction velocity. Thus a value of $u_{*CR} = 1.62$ cm s^{-1}, obtained from a curve giving the threshold of movement of sediment and corresponding to a grain size of 500 μm with $z_o = 0.5$ cm (Heathershaw, 1984), gives $u_{100_{CR}} = 21.46$ cm s^{-1}. q_{sb} is then calculated.

For the present work, q_{sb} is averaged over a complete tidal cycle, for any particular position, to give an indication of net sediment transport.

3 Results

3.1 Development of the model

Firstly it is necessary to find a suitable way of modelling the topography. Various profiles of the form H = A - B tanh (Cx - D) were tried, since these give qualitatively the correct behaviour. Here A, B, C and D are fitting parameters. However, it is difficult to produce a function which has a suitable slope gradient, reaches its level close enough to the slope area, and is level enough at the ends of the model not to invalidate

the radiation conditions. In preference a constant slope was chosen, sloping from a uniform on-shelf depth of 165 m at x = 150 km down to a uniform off-shelf depth of 4000 m at x = 100 km. This approximates to the available bathymetry for La Chapelle Bank. There is evidence from the results that the shape of the shelf-break has an effect on the steepness of the internal waves produced. For most of the work a barotropic tide of amplitude 0.45 m s^{-1} was used, this being an average value from current meter readings on La Chapelle Bank.

Tests were carried out to determine the effects of the constants K_1 and K_2 on the stability of the model. The model was initially tried with K_1 and K_2 both zero, and marked instabilities in the spatial profiles of the interface were observed on the same scale as the grid. Investigating K_1, keeping $K_2 = 0$, various values were tried and it was found that while values of the order of 10 m^2s^{-1} attenuated the instabilities somewhat without removing them, higher values of the order of 50 m^2s^{-1} smoothed the instabilities completely, but were found to attenuate the genuine internal waves more than one might expect diffusion to do in nature. Thus a compromise was required to smooth the instabilities as effectively as possible without affecting the waves of interest. However, since the instabilities only appeared to be generated at the shelf-break, a non-constant value of K_1 was tried. The idea was to have a peak value of K_1 just below the shelf break where smoothing was required, and have it tailing off to a much smaller value away from the shelf-break so as not to attenuate the propagating internal waves too rapidly. An exponential form for K_1 was found to be most suitable, viz:

$$K_1 = 30 + 270\, e^{-1.1 \times 10^{-9}(x - 90{,}000)^2} \quad m^2s^{-1} \qquad (18)$$

which has a peak value of 300 at x = 90 km, and tails away quickly to about 30. This provided very good stability.

In a similar way the effect of K_2 was investigated, but it was found that values large enough to smooth the instabilities even a little, for example $K_2 = 10^{-5}$ s^{-1}, also smoothed out the internal waves. It was concluded that K_2 was of little additional use in reducing instabilities, and so it was set to zero.

The parameters Δx and Δt also appear to play an important part in the stability of the numerical solution. Some work on this (Simons, 1980) was noted in section 2.4. At the stage where an exponential form of K_1 was being used the grid scales were Δx = 500 m and Δt = 300 s. However, in searching for velocity surges (see section 3.5) the expontential form of K_1, (18), was

found to be suppressing the features required, and was reduced again to a constant value of 40 $m^2 s^{-1}$. It was found that by halving the grid scales the instabilities virtually disappeared. Using a value of $K_1 = 40$ gave a ratio for the magnitude of the diffusion term relative to the other terms of the wave eqn, of the order of 10^{-3}.

The numerical stability of the model, however, seems to be best achieved by making the grid scales small since this does not effect the genuine internal waves. Small values of K_1 (< 50) may also be used to enhance stability.

The radiation conditions used (equation (8)) were not overly successful in allowing waves to pass freely out through the ends of the model. At the righthand (on-shelf) end of the model the imposed condition worked for a certain time before becoming unstable, while at the lefthand (off-shelf) end the model became unstable almost as soon as waves reached it, causing the breakdown of the method. The only solution to this problem was found by extending the boundaries beyond the range of the waves in whatever time period was chosen for the model to run. This meant that in practical terms the model could not be run for more than 48 hours. However, this was not serious since the model always reached a steady state within this time (see section 3.2).

As noted in section 2.2 Pingree et al have omitted from their momentum equation (equation (6)) the term:

$$\frac{1}{2} \frac{\partial}{\partial x} \left(u^2 \frac{(h_2 - h_1 + 2\eta)}{H} \right)$$

This term was included in the present model to investigate its importance. Removing it was found to make an observable but slight difference. Thus its inclusion appears to be unimportant.

3.2 Wave motion predicted by the model

Before examining the wave motion predicted by the model, it was necessary to find the most realistic values of h_1 and $\delta\rho$. C.T.D. data from La Chapelle Bank provided average values of about 50 m for h_1 and about 6×10^{-4} g cm^{-3} for $\delta\rho$.

The basic pattern of wave motion resulting from a barotropic tidal flow over the continental shelf topography described is illustrated in Figs 4 and 5. Fig 4 illustrates the displacement of the boundary by six profiles equally spaced over one whole tidal cycle, while Fig 5 illustrates the displacement of the boundary by 12 profiles equally spaced over one tidal cycle, and each

displayed separately. Exactly the same conditions apply in both. The motion can be seen to be centred around the shelf break, and could be summarised by saying that the interface at the shelf break oscillates up and down with the period of the barotropic tide, and from this oscillation progressive internal waves propagate in both the off-shelf and on-shelf directions. Note the asymmetries in both. The bunching seen on the on-shelf side in Fig 4 is due to the oscillating barotropic tide alternately speeding up and slowing down the propagating waves; on the off-shelf side the tidal flow is not sufficient to cause any noticeable effect. The waves decrease in amplitude as they propagate in both directions, this being due to attenuation by the diffusion term K_1.

The model settles down to a steady state after three tidal cycles, and it is this steady state which is shown in Figs 4 and 5. However, when the model is started from rest the first wave which propagates in each direction is both larger in amplitude than the subsequent ones, and travels faster. This is presumably because the wave is propagating into a flat interface rather than following a train of waves.

With a motion such as that described, tests were done on the speeds of the waves, comparing their positions as predicted by the model with the successive positions that would be predicted by long wave theory. This was done by calculating the long wave phase speed, adding it to the appropriate barotropic tidal velocity and integrating with respect to time. Apart from the first wave in each direction when the model is started, which as already mentioned goes faster than the rest of the waves, all the others seem to tie in well with the long wave prediction within the bounds of measuring errors. Table 1 shows the results of one such calculation.

Table 1

Predicted and measured wave crest positions for a wave propagating on-shelf

$h_1 = 50$ m $\qquad \delta\rho = 8 \times 10^{-4}$ g cm^{-3}

Common starting position = 160.2 km

Positions obtained from the numerical model (km)	Positions predicted by integration of long wave and tidal velocities (km)
160.2	160.2
167.2	166.9
171.6	171.2
173.0	172.7
174.1	173.7
178.0	176.8
184.0	182.9
191.0	189.8

Initially there seems to be a slight acceleration of the modelled wave relative to the long wave prediction, but in each case this settles down by the end of the third tidal cycle the model has been running. The grid scale of the model limits the accuracy with which crest positions can be located, and within the limits of accuracy the waves seem to follow the predictions reasonably well.

3.3 Explanation of the wave motion in terms of steady flows

In an attempt to simplify some of the development stage, the model was run once or twice with steady flows rather than oscillating tidal flows. The results of these experiments provide a useful insight into the motion observed for a tidal flow. Figs 6 and 7 are two such results. Both of them show the position of the interface at 2 hour intervals after a steady current of 0.2 m s^{-1} is 'switched on'. In Fig 6 this is an off-shelf current, and in Fig 7 an on-shelf current. Fig 6 shows a relatively sharp depression occuring in the interface at the shelf break. From this depression of the interface a single 'surge' propagates in each direction with constant speed, leaving, as it propagates away, the interface at a lower level, the on-shelf (upstream) side being lower than the off-shelf (downstream) side. Fig 7 is very similar, only as one would expect the displacement is now upwards. The larger displacement is still on the upstream (now off-shelf) side of the shelf break.

Very broadly, the sinusoidally varying barotropic tide may be thought of in terms of an off-shelf flow being 'switched on', then 6 hours later this flow being 'switched off' and an on-shelf flow being 'switched on' and so on. Clearly this is not exactly the situation, but alternating every half tidal cycle the situations seen in Figs 6 and 7 can be seen to add up to the kind of motion seen in Fig 4, not only in the way waves are generated at the shelf break and propagate outwards, but also in the way that the mean displacement of the envelope is higher on the off-shelf side than it is on the on-shelf side.

More properly the sharp crest which forms during the off-shelf current is an internal wave with an on-shelf phase speed, and so propagates onto the shelf when the current relaxes. The opposite happens during the on-shelf current with the peak that forms in the interface.

3.4 Influence of h_1 and $\partial\rho$

h_1, the upper layer depth, and $\partial\rho$, the density difference, are two physical factors which can vary considerably, and tests were done to find their effect on

the wave pattern described in 3.2 Data measured from La Chapelle Bank at various times of the year suggests that sensible ranges for these two parameters would be h_1 between 30 and 70 m, and $\partial\rho$ between 4×10^{-4} and 12×10^{-4} g cm^{-3}. Fig 8 shows the spatial picture (as in Fig 4) for various combinations of h_1 and $\partial\rho$ in these ranges, only in this case the envelopes of the curves alone have been shown, simply for clarity. This table of graphs serves as a summary of the effects of both these parameters. The general trend is that as $\partial\rho$ increases so the amplitude of the central peak decreases[+], but at the same time the amplitudes of the propagating waves increase[++], and as would be expected the speed of propagation of the waves increases. As h_1 increases the amplitudes both of the central peak and of the propagating waves increase, and the speed of propagation increases, though not as noticeably as with $\partial\rho$. h_1 seems to have the most marked effect on amplitude, and $\partial\rho$ the most marked effect on phase speed.

Investigating the maximum wave height over the whole tidal cycle for various values of h_1 and $\partial\rho$ it was discovered that for values of $\partial\rho$ less than about 3×10^{-4} g cm^{-3} the model did not behave as expected. Clearly there can be no internal waves if there is no interface ($\partial\rho = 0$), and as the model approaches $\partial\rho = 0$ it might be expected to become invalid.

3.5 Investigation of velocity surges

To this end the motion in the system was examined with respect to time, rather than to horizontal displacement, and in particular the upper and lower layer velocities u_1 and u_2. Fig 9 shows u_1 and u_2 plotted against time for various positions near the shelf-break; the broken line in each case represents the barotropic tide. Comparing this with Fig 1, where the depth of the upper layer is approximately 50 m, it can be seen that the model has successfully predicted the observed surges, these being positive (on-shelf) in the upper layer and simultaneously negative (off-shelf) in the lower layer. The plot for 6 km on-shelf in Fig 9 corresponds to the data in Fig 1, and shows the surge occurring about 1 hour before maximum flood, which is very similar to the surges in Fig 1. The largest surge is seen at the shelf-break, and in the lower layer this could have a very important effect on sediment transport (see section 3.7).

As can be seen in Fig 9, as the wave propagates on-shelf, its effect is

---

[+] The interface requires more energy to be displaced by a given amount for larger $\partial\rho$

[++] Presumably because the waves, travelling faster, reach a given position sooner and so have had less time to "diffuse" according to K1 in eqn 6.

felt later at each successive position. At about 18 km onto shelf, however, each internal tide encounters a barotropic ebb current so that its passage time is greatly increased. The surge is thus drawn out and is much less noticeable. However, at about 25 km onto shelf the wave is advected with the ensuing flood tide and again appears as a characteristic surge.

3.6 Influence of h_1 and $\delta\rho$ on velocity surges

Having investigated the effects of these two parameters on the spatial picture produced by the model, it is also interesting to investigate their effect on the velocity surges described in the previous section. Running the model as for Fig 9, only with different h_1 and $\delta\rho$ values, indicates that in general the amplitude of the surge is not significantly altered by $\delta\rho$, although increasing $\delta\rho$ does increase its duration[+]. On the other hand surge amplitude increases markedly with h_1, but with no significant change in its duration. This is because, as noted in section 3.4, the effect of h_1 on the waves was to increase their amplitude but to have less effect on their speed.

Since the surges occur simultaneously in both layers, and are of opposite sign, the shear u, or baroclinic tide, will also show a marked surge at the same point. Thus taking the maximum absolute shear value over a whole tidal cycle gives a measure of the amplitude of these surges. This has been plotted as a function of horizontal position (for a region around the shelf break) in Fig 10, showing what happens as $\delta\rho$ varies for fixed h_1 = 50 m in Fig 10a, and as h_1 varies for fixed $\delta\rho = 6 \times 10^{-4}$ g cm^{-3} in Fig 10b.

Fig 10a shows that, away from the shelf-break, the larger the $\delta\rho$ the larger the surge amplitude. This is partly due to the fact that (as remarked earlier in connection with Fig 8) the larger the $\delta\rho$, the larger the wave amplitudes away from the shelf-break. However, the dominant factor is probably that larger $\delta\rho$ values produce faster travelling waves, which (from grounds of mass conservation) must be associated with larger shear values (for equal wave amplitudes).

Fig 10b shows surge amplitude increasing everywhere with upper layer depth, but most noticeably so at the shelf-break.

The general shape of each of the curves is also interesting to note, expecially the sudden increase in surge amplitude from 1 km off-shelf to the shelf-break. The diagram in Fig 11 illustrates what is happening as a wave generated just off-shelf propagates over the shelf-break. Water from the on-shelf lower layer is forcibly 'squeezed' off the shelf, the more so if the

---

[+]Probably because, as $\delta\rho$ increases, the wave, travelling faster, arrives (at say 156 km) earlier in the tidal cycle when the flood is less strong, and takes longer to advect past the fixed position

interface is near the bed. This would explain why Fig 10 shows such a sudden peak at the shelf-break[+], why this is more pronounced for larger h_1, and why Fig 9 shows the largest surge at the shelf-break.

3.7 Implications for sediment transport

The last point about the accelerated flow at the shelf-break could have implications for sediment transport. It might be expected that such a surge of water over the shelf-break would be responsible for moving a considerable amount of sediment. The calculations to evaluate tidally averaged values of q_{sb}, $\overline{q_{sb}}$ say, support this, although the quantity of sediment moved is perhaps not quite as much as might be expected. However, it must be borne in mind that the off-shelf surge in the lower layer at the shelf-break only lasts for less than half a tidal cycle. Fig 12 shows the values calculated using $h_1 = 50$ m and $\delta\rho = 6 \times 10^{-4}$ g cm^{-3} at various positions in the shelf-break region. For all h_1 and $\delta\rho$ a sharp peak value of $\overline{q_{sb}}$ is seen at the shelf-break itself. In Fig 12 this value is about .008 g cm^{-1} s^{-1}. This peak value seems to be insensitive to $\delta\rho$, but varies considerably with h_1 from virtually zero with $h_1 = 30$ m to something of the order of 0.04 g cm^{-1}s^{-1} for $h_1 = 70$ m.

Examining the values of $\overline{q_{sb}}$ varying with position, as in Fig 12, an interesting pattern is observed. Although nowhere outside about 1 km of the shelf-break is $\overline{q_{sb}}$ more than .002 g cm^{-1}s^{-1}, at most positions it is observed to be on-shelf in direction, while every 10 km or so it becomes off-shelf for about 2 km. Clearly sediment transport on the off-shelf side due to the internal waves is negligible.

As a further investigation, the total on-shelf depth was increased from 165 m to 180 m, to model sediment transport in a neighbouring area of La Chapelle Bank. Keeping h_1 the same, it was found that the shelf-break values of $\overline{q_{sb}}$ were approximately halved.

4 Conclusion

The model supports the existence of velocity surges observed at La Chapelle Bank. Furthermore it predicts that these surges, most pronounced at the shelf-break, may be responsible for transporting significant quantities of sediment over the shelf-break into the deep ocean.

[+]Because $u = u_1 - u_2$ and u_2 is made more negative by the passage of the wave

Appendix : Symbols used in the text and in the computer program

Symbol in text	Variable name in computer program	represents:
h_1	H	upper layer depth
h_2	(HH-H)	lower layer depth
H	HH	total depth (= h_1 + h_2 if ζ neglected in comparison to η)
ζ		displacement of surface
η	Y	displacement of interface
u_1	U1	velocity of upper layer
u_2	U2	velocity of lower layer
u	U	baroclinic or shear velocity = $u_1 - u_2$
U	UU	barotropic tide
x	X	horizontal displacement
t	T	time
ρ_1		density of upper layer
ρ_2	RHO2	density of lower layer
$\delta\rho$	DRHO	$\rho_2 - \rho_1$
h'		depth of displaced upper layer
h''		depth of displaced lower layer
K_1	K1	arbitary diffusion constant
K_2	K2	arbitary friction constant
β	BETA	$= \frac{g\delta\rho}{\rho_2}$
c	C1	long wave phase speed (off-shelf end
	CN1	(on-shelf end
Δx	DX	grid spacing for x
Δt	DT	grid spacing for t
N	N	an even integer - number of Δx grid spacings
U_o	UUØ	U at on-shelf end of model
H_o	HHØ	H at on-shelf end of model
	YNEW	)
	YOLD	) values of η and u at previous and next timestep
	UNEW	)
	UOLD	)
q_{sb}	QSB	bedload transport
$\overline{q_{sb}}$	QSBAV	tidally averaged q_{sb}
k	A	dimensional coefficient

Symbol in text	Variable name in computer program	represents:
d	D	grain diameter in mm
u_{100}	B	velocity 1 m above bed
$u_{100_{CR}}$	C	critical value of u_{100} for sediment transport to occur
κ	KAPPA	Von Karman constant
z_o	ZØ	roughness length
z		height above bed
u_*		friction velocity
u_{*CR}	USTCR	critical friction velocity
	U2CR	critical value of u_2 for sediment transport
	1MAX	number of time intervals program runs for
A)		
B)		Fitting parameters for shelf-break profile
C)		
D)		

N.B. For convenience and for comparisons with other work, all sediment transport calculations are in c.g.s. units, while all other calculations are performed in m.k.s. units.

References

BAGNOLD, R A, 1966. An approach to the sediment transport problem from general physics. US Geological Survey Professional Paper 422-I, 37p.

HARDISTY, J, 1983. An assessment and calibration of formulations for Bagnold's bedload equation. Journal of Sedimentary Petrology, 53, pp 1007-1010.

HEATHERSHAW, A D, 1984. Some observations of internal wave current fluctuations at the shelf-edge and their implications for sediment transport. Continental Shelf Research (in press).

HEATHERSHAW, A D and CODD, J M, 1984. Depth Controlled changes in grain size and carbonate content on a shelf-edge sand bank. Geo-Marine Letters (in press).

PINGREE, R D, GRIFFITHS, D K and MARDELL, G T, 1983. The structure of the internal tide at the Celtic Sea shelf break. J. Mar. Biol. Ass., UK, 64, pp 99-113.

SIMONS, T J, 1980. Circulation models of lakes and inland seas. Can. Bull. Fish. Aquat. Sci, 203 : 146p.

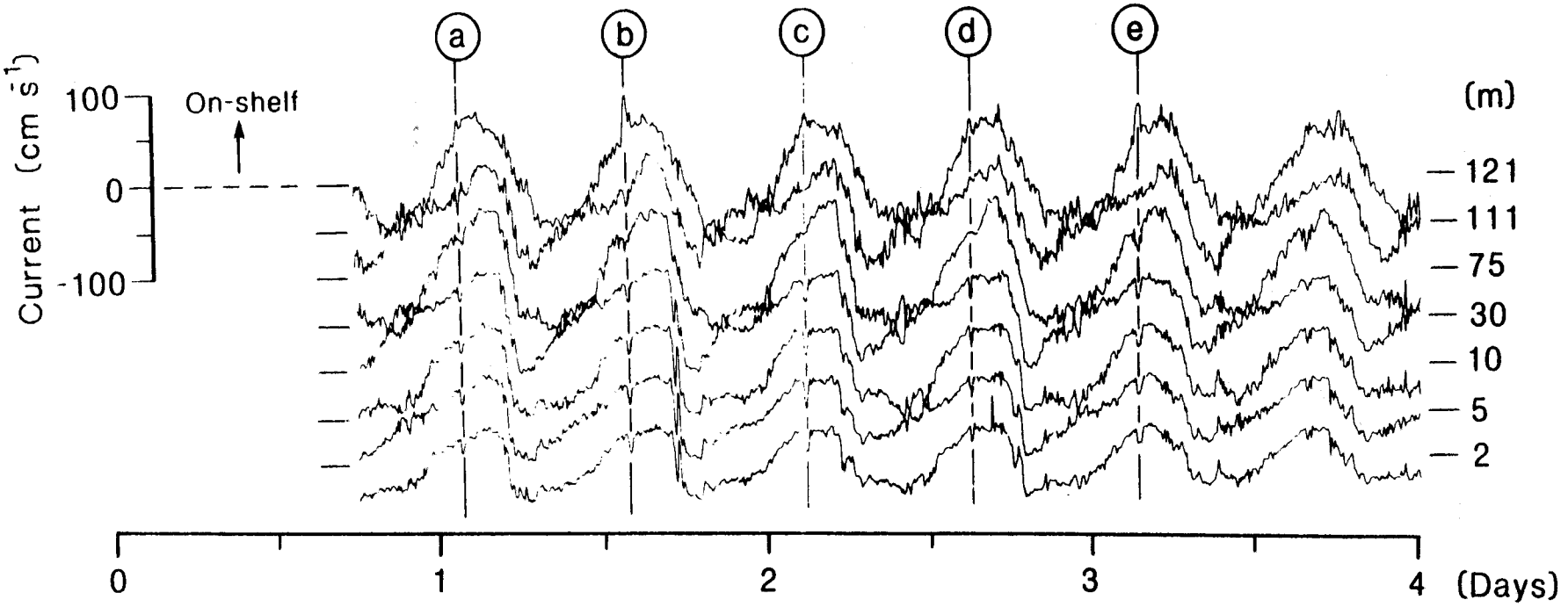

Figure 1 Current measurements from La Chapelle Bank showing velocity surges about 1 hour before maximum flood (labelled a, b, c, d, e). These measurements were taken about 6 km on-shelf. Taken from Heathershaw (1984).

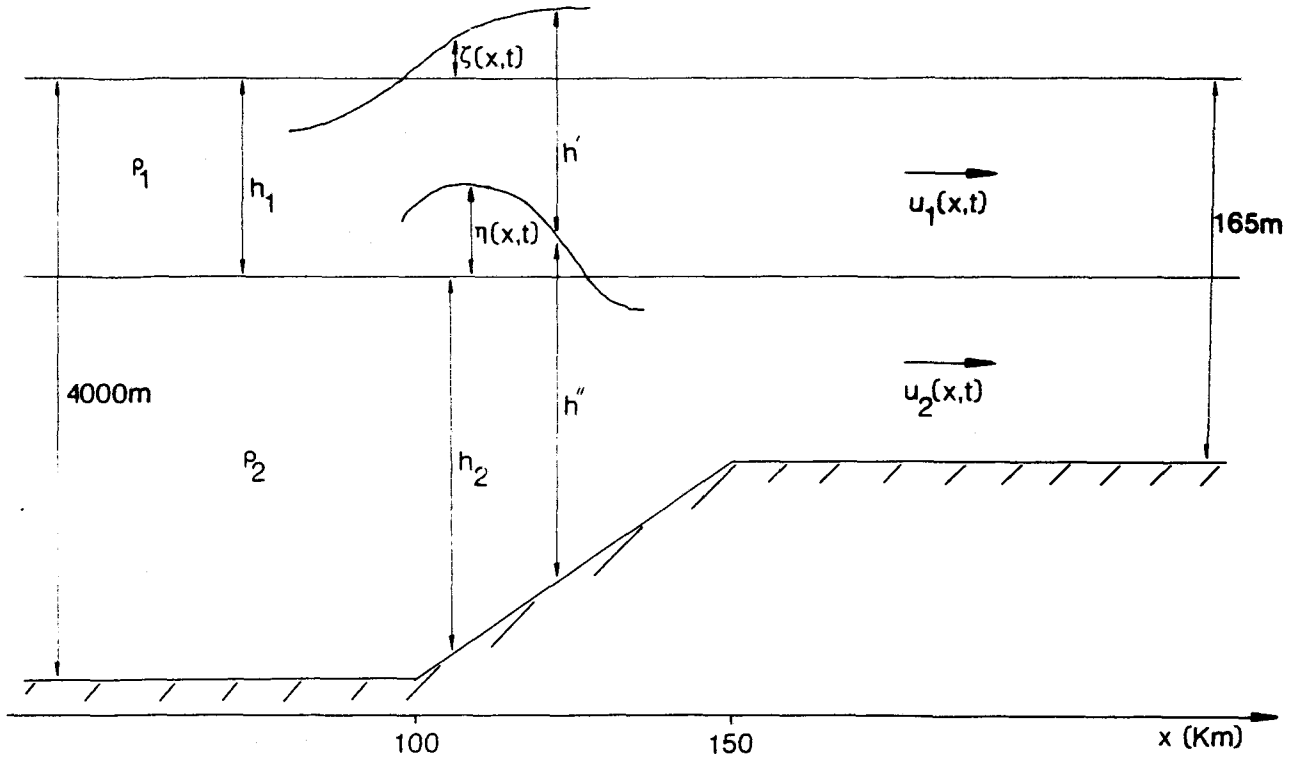

Figure 2 Diagram of the topography used for the model, and also showing the variables used in the model.

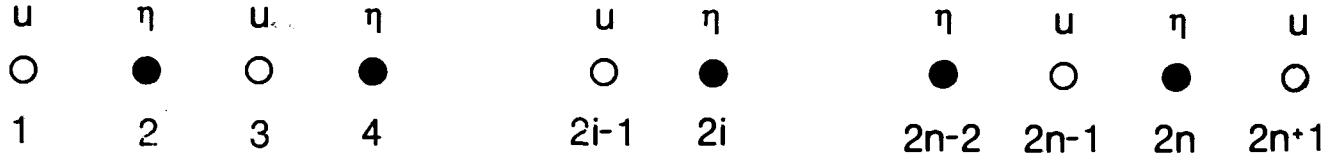

Figure 3 Diagram showing how a space staggered solution is produced from the timestepping process. Intermediate values are then obtained by linear interpolation.

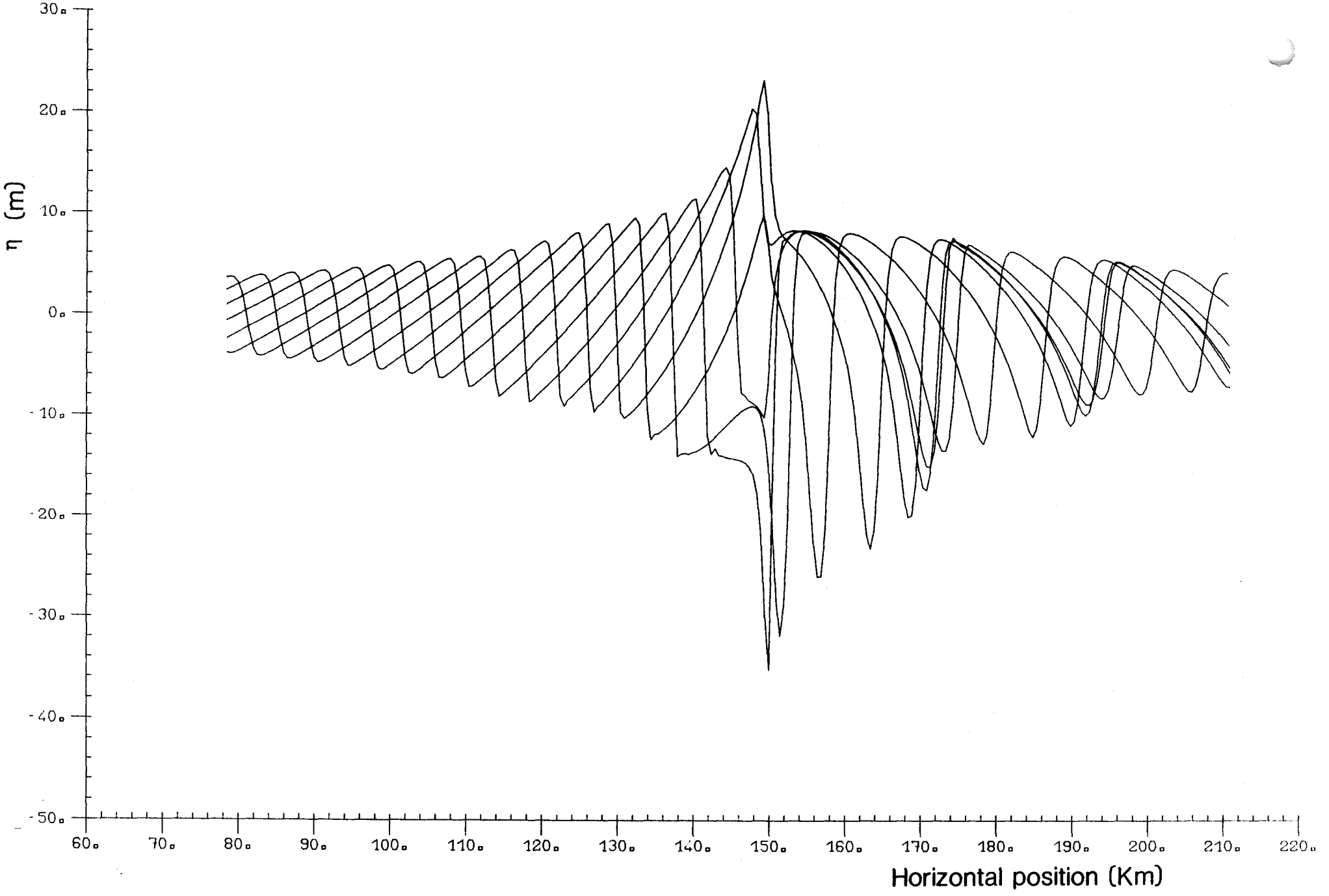

Figure 4 Displacement of the interface at six succesive intervals of approximately 2 hours. Thus one whole cycle is represented here.
($\delta\rho$ = 6 x 10^{-4} g cm^{-3}, h_1 = 50 m)

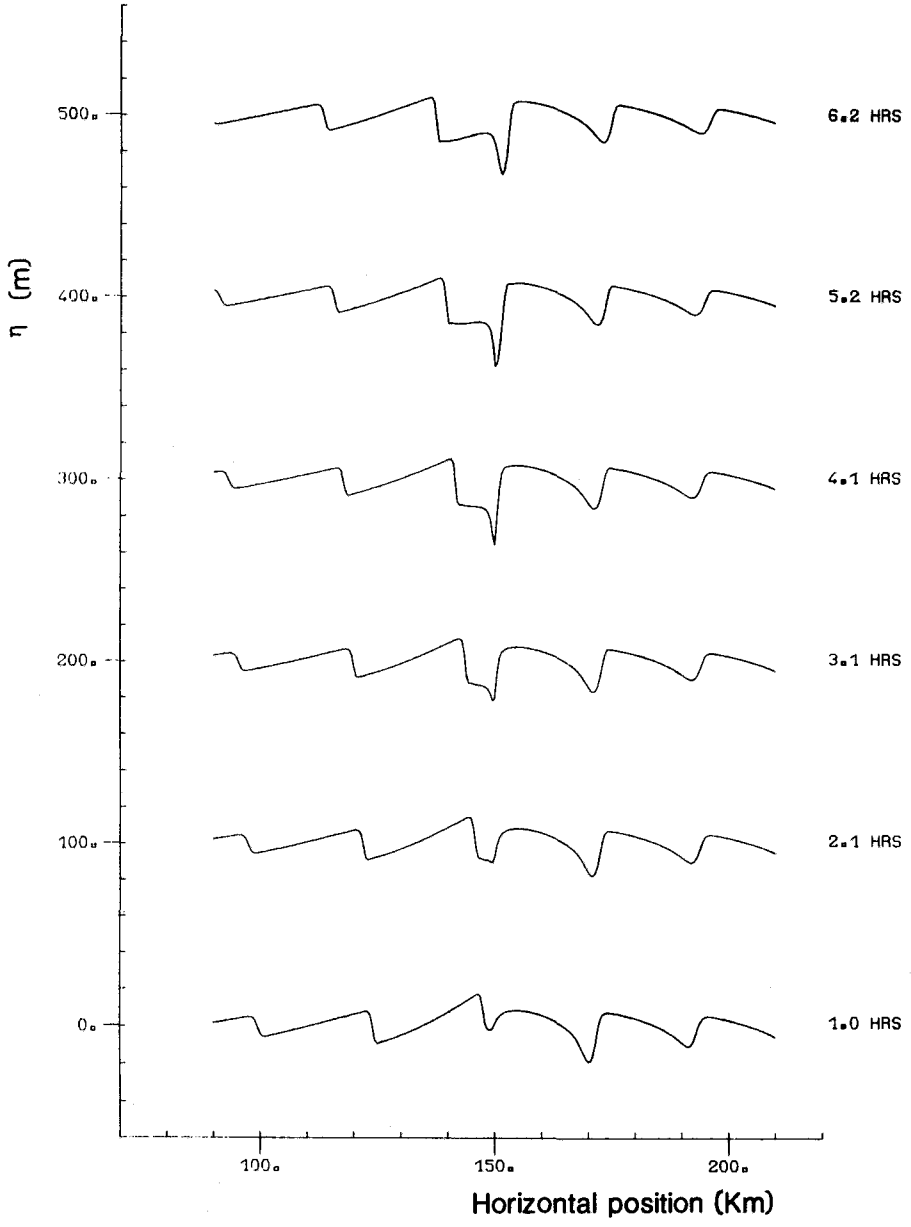

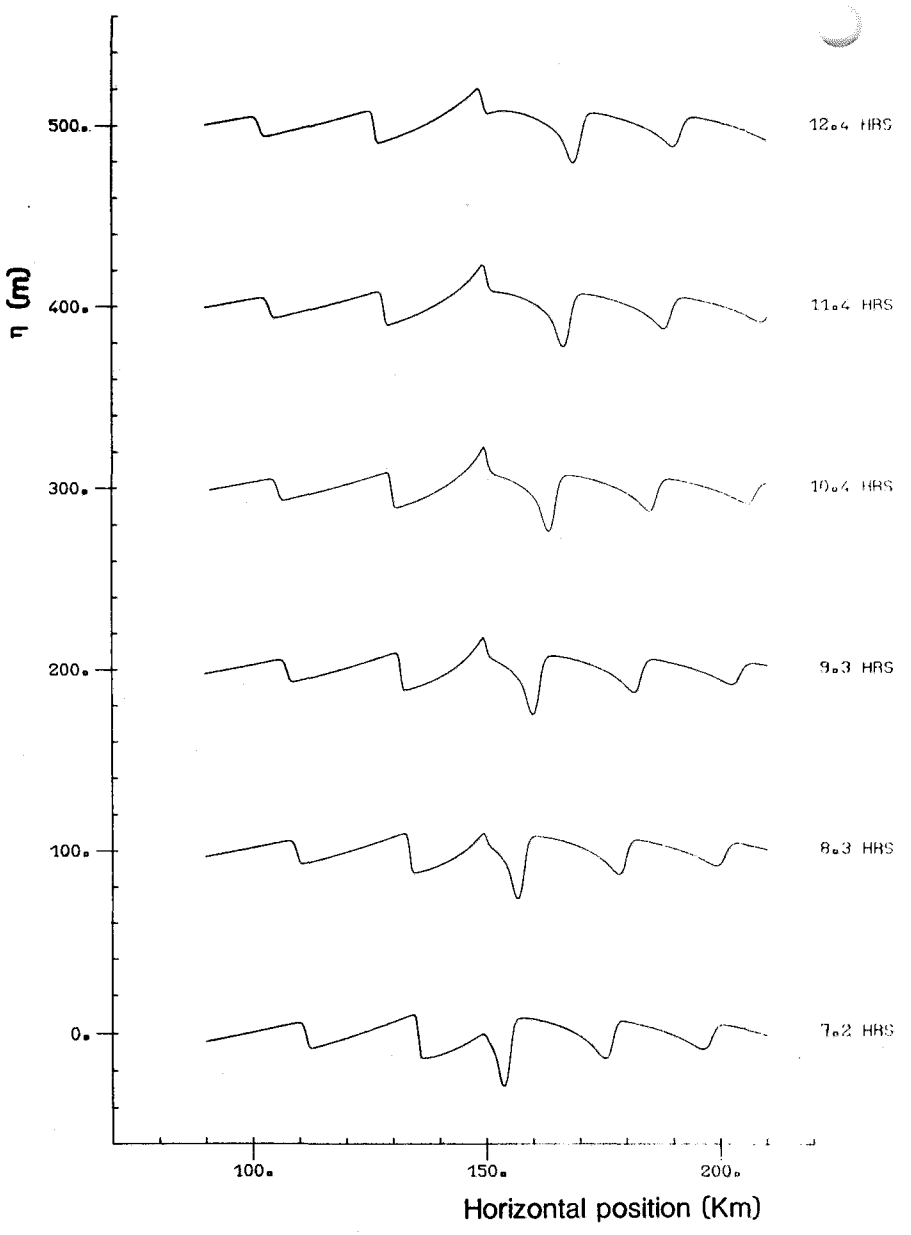

Figure 5 Displacement of the interface at twelve successive intervals of approximately 1 hour. One whole tidal cycle is represented. ($\delta\rho$ = 6 x 10^{-4} g cm^{-3}, h_1 = 50 m). Successive plots displaced by 100 m.

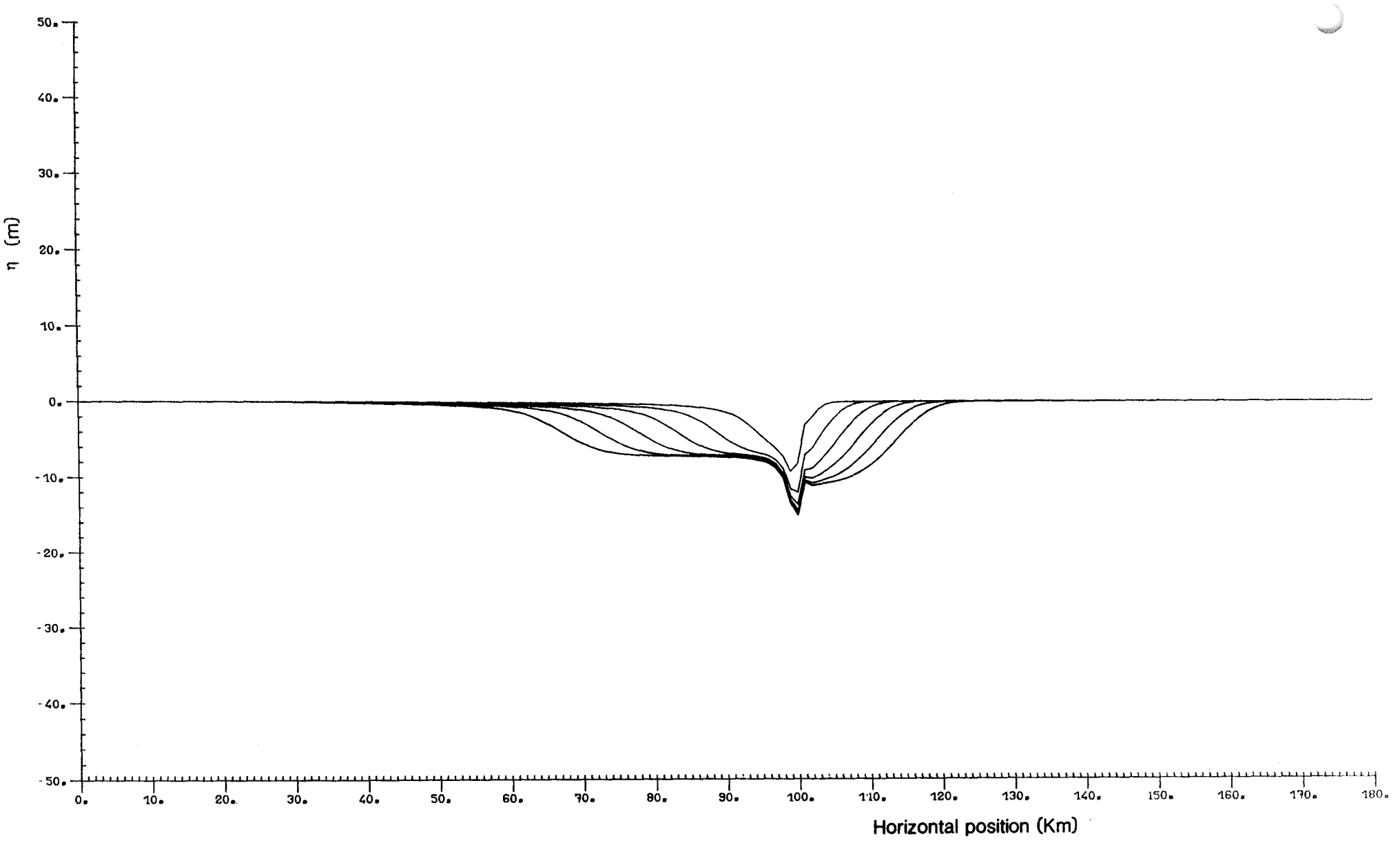

Figure 6 Steady flow of 0.2 m s^{-1} off-shelf, starting at time t = 0. Position of interface shown here at 2 hour intervals for the first 12 hours. ($\delta\rho$ = 8 x 10^{-4} g cm^{-3}, h_1 = 50 m)

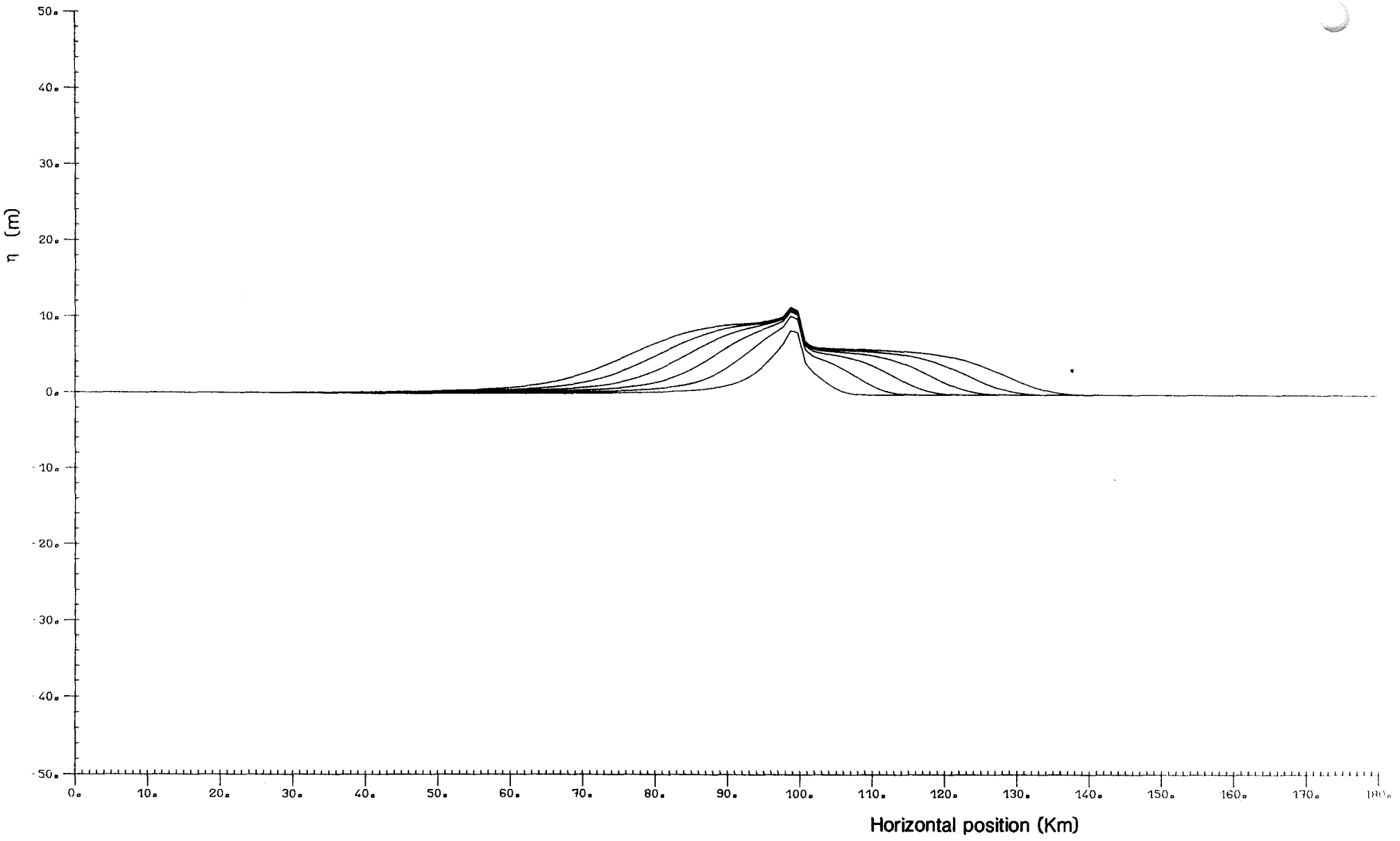

Figure 7 Steady flow of 0.2 m s^{-1} on-shelf, starting at time t = 0. Position of interface shown here at 2 hour intervals for the first 12 hours. ($\delta\rho$ = 8 x 10^{-4} g cm^{-3}, h_1 = 50 m)

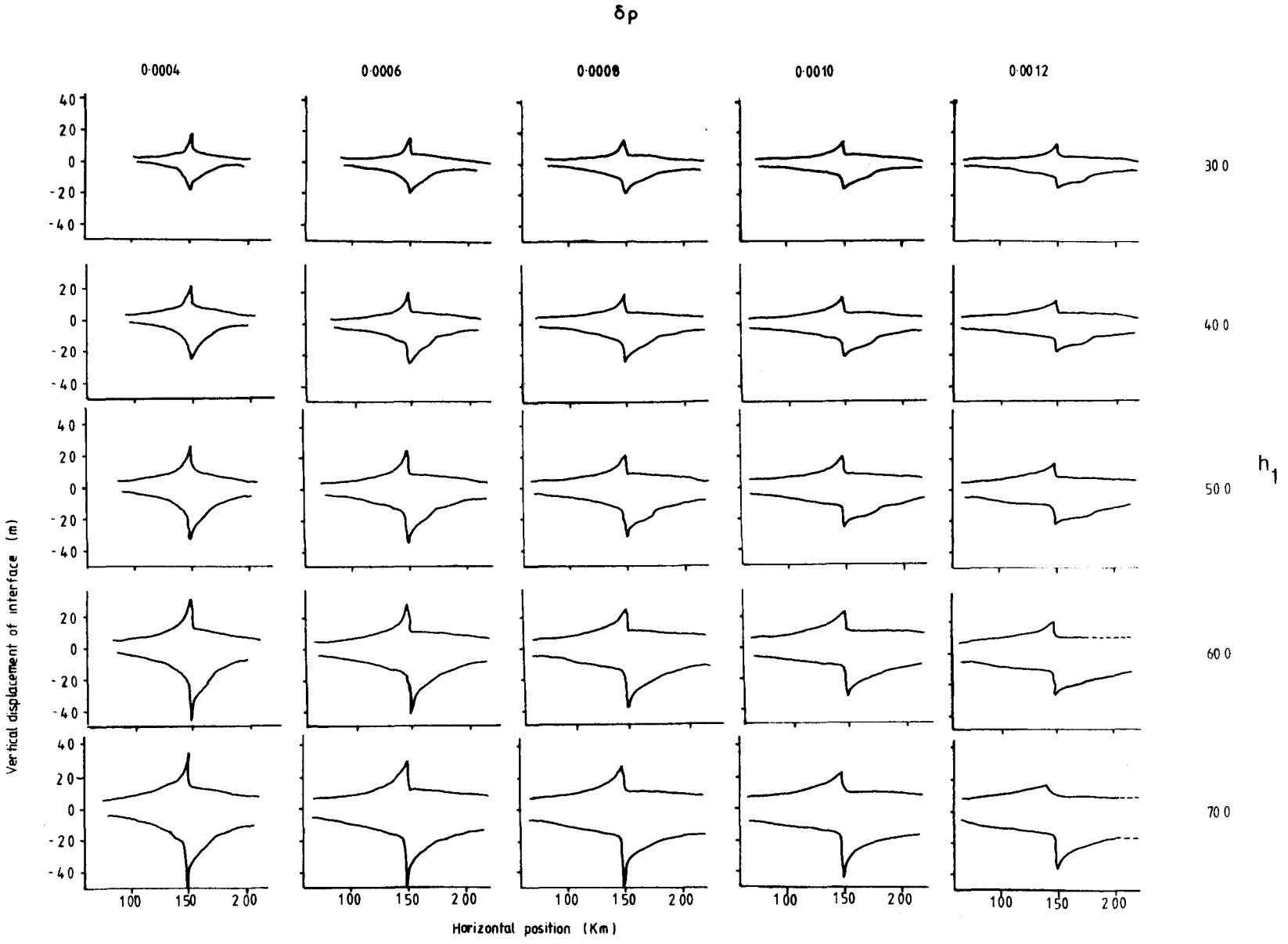

Figure 8 Envelopes of interface displacement curves for varying $\delta\rho$ and h_1.

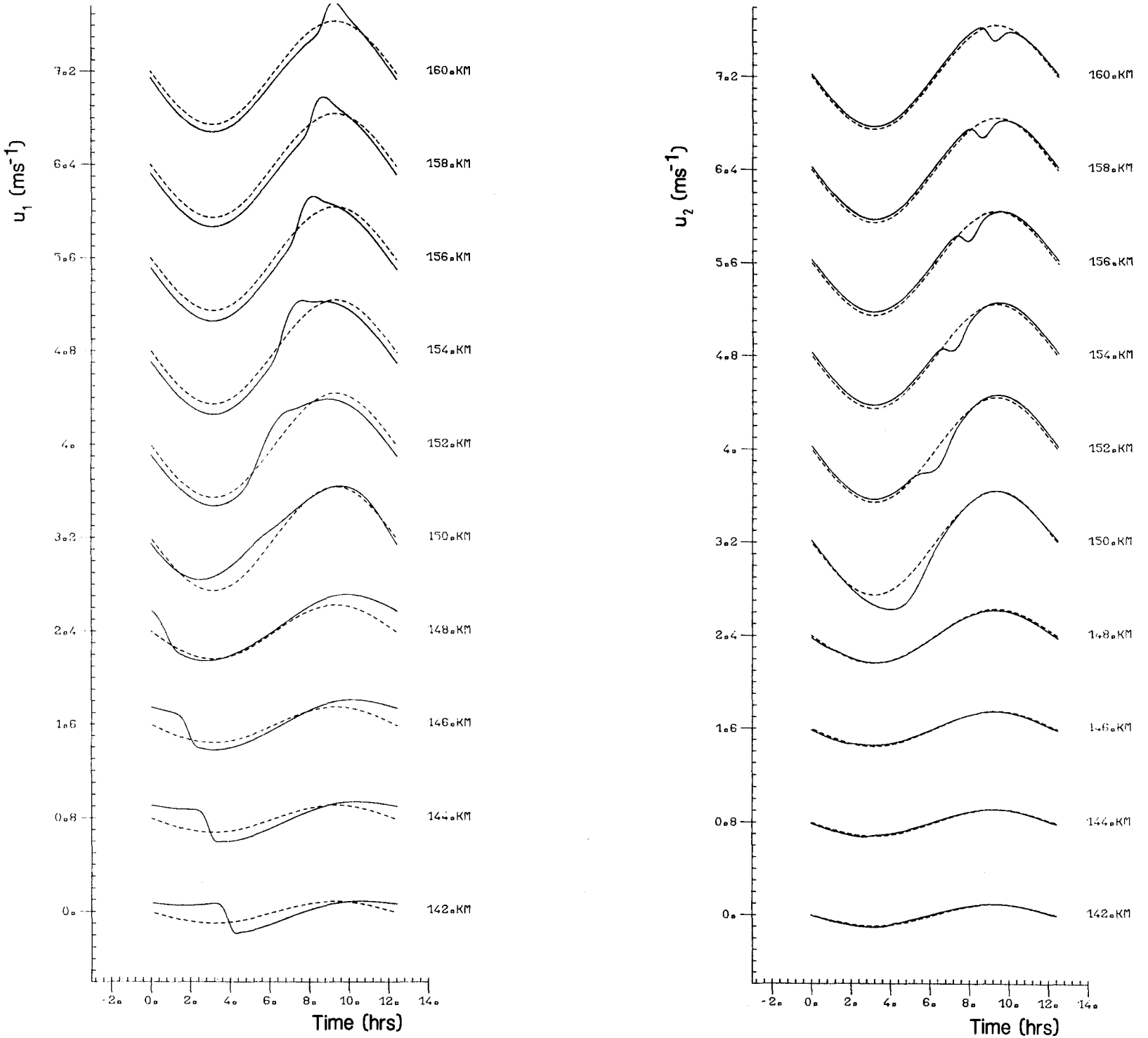

Figure 9 Variation of U_1 and U_2 over one tidal cycle. Shown for various positions near the shelf break. The dotted lines are the barotropic tide at each position. Successive plots displaced by 0.8 m s^{-1}.

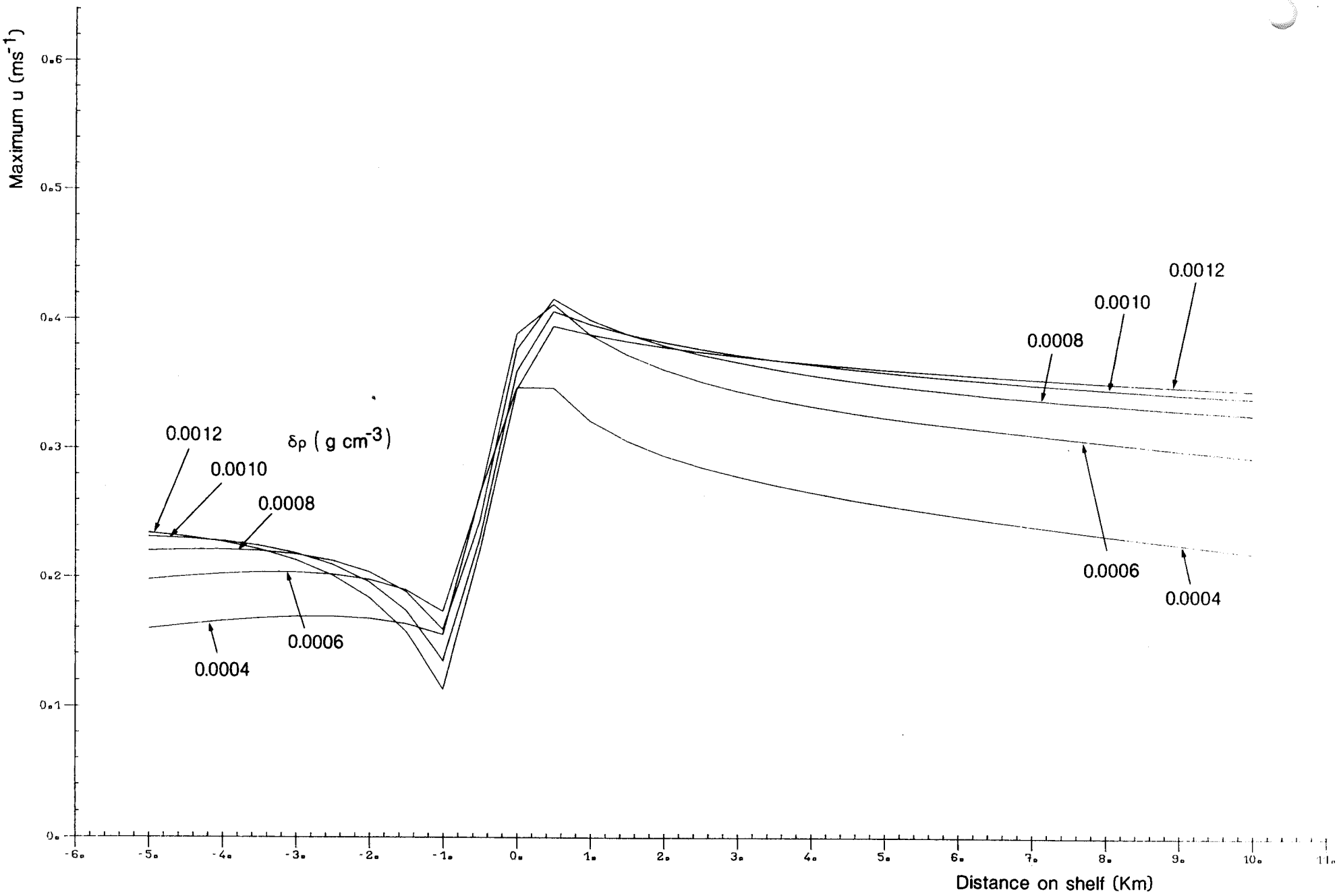

Figure 10a Maximum shear, a measure of surge amplitude, plotted against distance on-shelf for successive values of $\delta\rho$. (h_1 = 50 m)

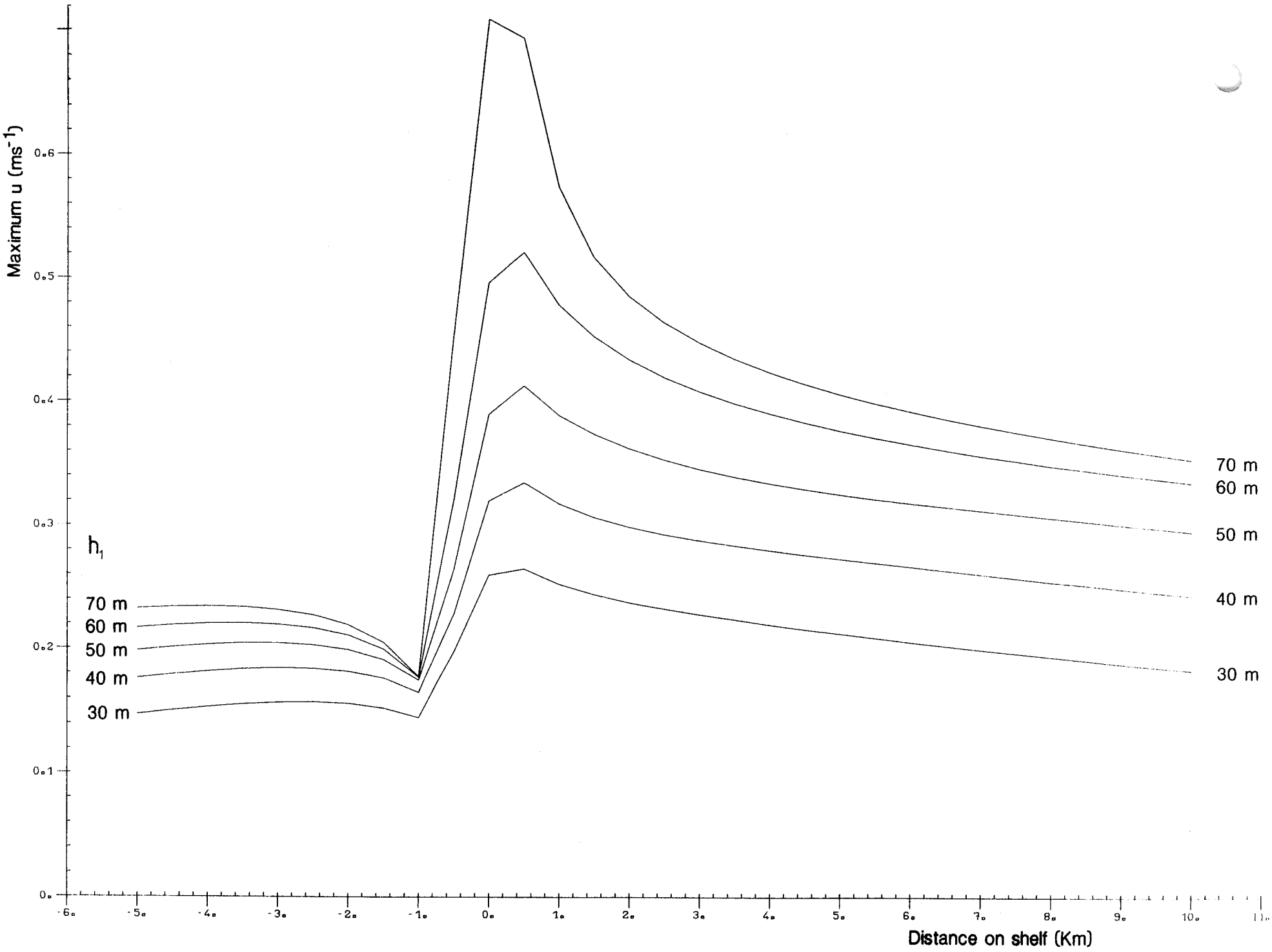

Figure 10b Maximum shear, a measure of surge amplitude, plotted against distance on-shelf for successive values of h_1. ($\delta\rho$ = 6 x 10^{-4} g cm^{-3})

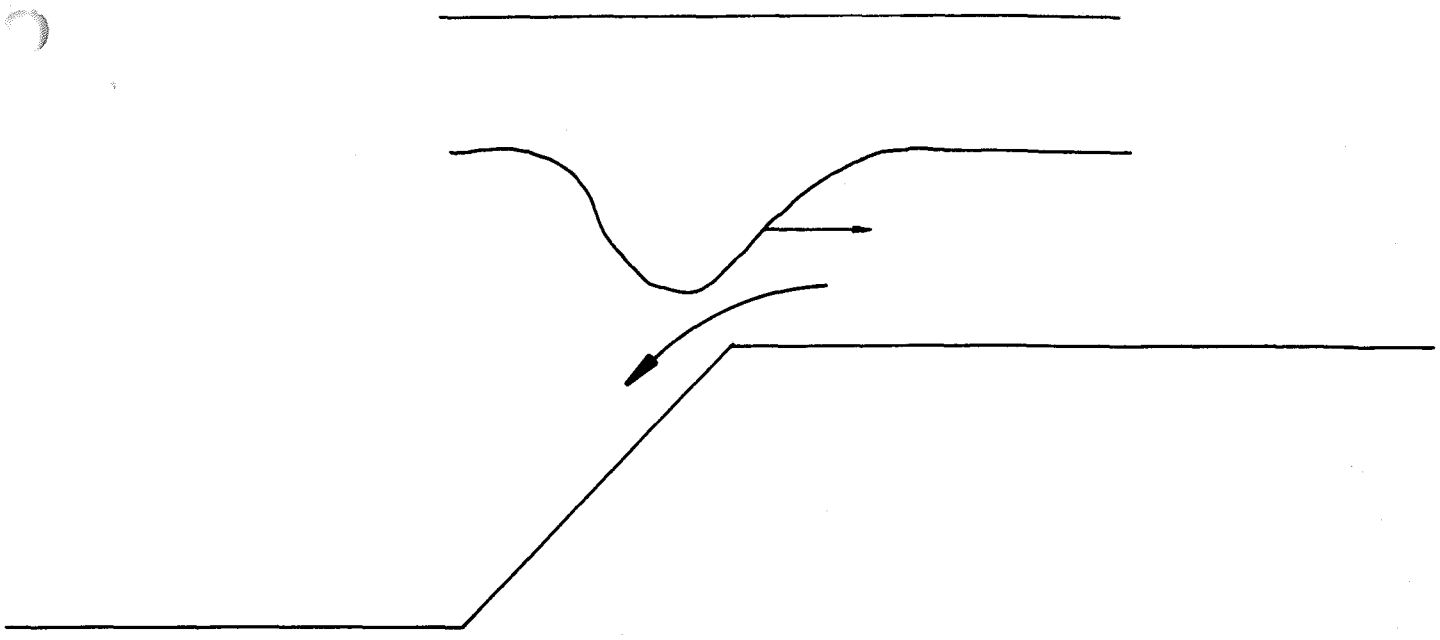

Figure 11 Diagram showing how a wave propagating on-shelf causes a large off-shelf surge in the velocity of the lower layer at the shelf break due to a 'squeezing' effect.

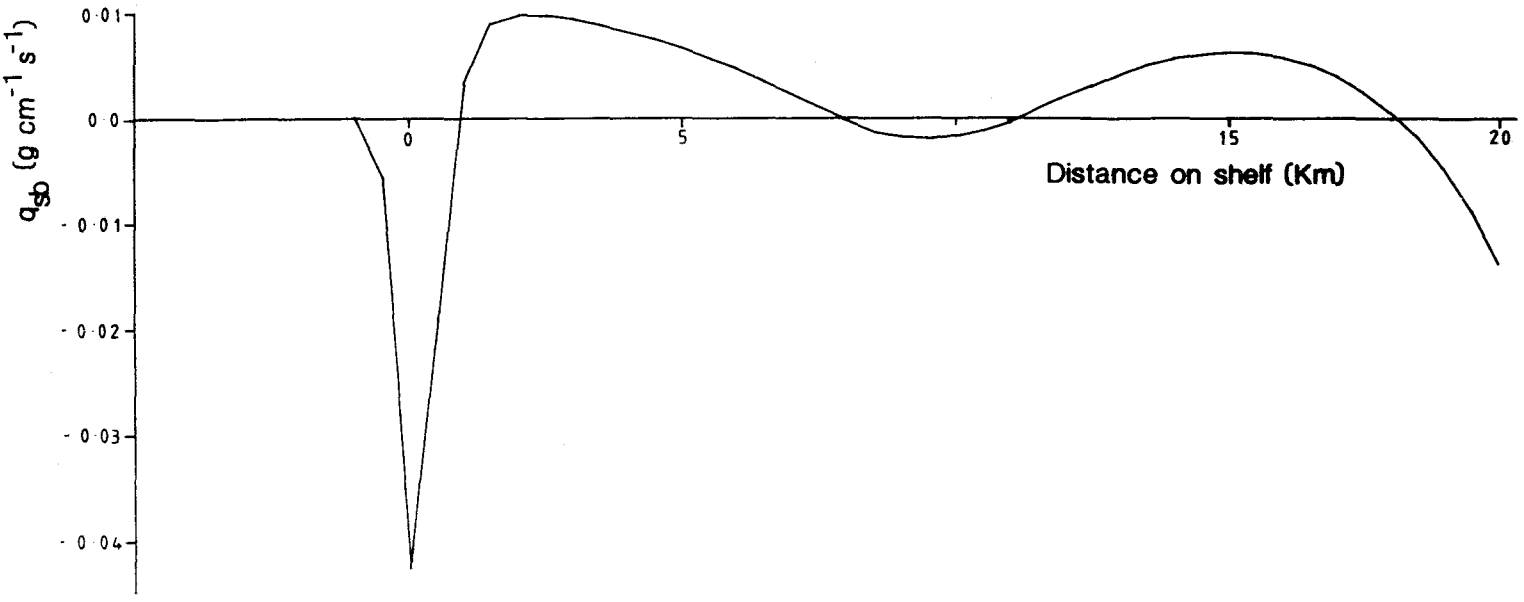

Figure 12 Tidally averaged bedload transport rates, $\overline{qsb}$, for positions in the shelf break region. ($\delta\rho$ = 6 x 10^{-4} g cm^{-3}, h_1 = 50 m)